LRP 456/92 May 1992

Papers contributed to the
19th EPS CONFERENCE ON CONTROLLED
FUSION AND PLASMA PHYSICS

Innsbruck, Austria,
June 29th - July 3rd, 1992

Ideal-MHD Operational Limits for Highly Elongated Tokamaks

G. Eriksson*, A. Bondeson, D.J. Ward, F. Hofmann and L. Villard

Centre de recherches en physique des plasmas, Association Euratom - Confédération Suisse, Ecole polytechnique fédérale de Lausanne, Lausanne, Switzerland

I. INTRODUCTION

The construction of strongly shaped and elongated tokamaks is to a large extent motivated by the theoretical prediction that the beta-limit is proportional to the plasma current [1]. Experimental results confirm the advantageous effects of increased elongation ($\beta = 11\%$ was reached with an elongation $\kappa = 2.34$ in DIII-D [2]). The understanding of beta and other operational limits at very high elongation ($\kappa > 2.5$) is, however, very limited. Notably, it is not clear whether the beta limit can be further increased by an increase in κ or by other types of shaping, whether vertical stability limits the achievable elongation and whether control of current and pressure profiles is necessary.

We report on an ideal MHD stability study in progress with the aim of clarifying the operational limits imposed by n = 0 (vertical), 1 (kink) and ∞ (ballooning) stability for tokamaks with elongation from 2 to 3, in particular, for shapes accessible to the TCV tokamak in Lausanne. The shape of the plasma-vacuum boundary is prescribed as:

$$R/a = A + \cos(\theta + \delta \sin\theta + \lambda \sin 2\theta) \quad , \quad Z/a = \kappa \sin\theta \ .$$

The parameter λ modifies the shape of the tips: $\lambda > 0$ makes the tips broader. We refer to configurations with $\delta = 0.5$ and $\lambda = 0.2$ as "TCV dee". For all results presented here, the aspect ratio is A = 3.7. Generally, the current profiles are prescribed, and unless otherwise stated, q_0 is held fixed at 1.05. The pressure profiles are either prescribed or optimized at the ballooning limit (in the first stability region). Critical betas are then computed for n = 0 and n = 1 stability with the pressure profile a scaled version of that which gives the ballooning limit. The n = 0 modes are calculated for a resistive wall with the shape of the TCV vacuum vessel. We assume that the n = 0 mode can be stabilized by active feedback if the growth time in the absence of feedback is longer than 0.5 ms. The n = 1 limits do not take into account wall stabilization. The equilibria, n = 0 and n = 1 modes are computed with the CHEASE [3], NOVA-W [4] and MARS [5] codes, respectively.

II. CURRENT AND INDUCTANCE LIMITS AT ZERO PRESSURE

It is well known that the circular current limit $q_\psi \geq 2$ does not apply for sufficiently noncircular equilibria (including those with X-points). Figure 1 shows the limit in normalized current $I_N = \mu_0 I_p / aB_0$, set by n = 1 stability at zero pressure, as a function of q_0 for different shapes ($\delta = 0.25$, 0.5 and $\lambda = 0$, 0.25) and elongations $\kappa = 2.5$ (1a) and $\kappa = 3.0$ (1b). Here we use a simple current profile: Rj_ϕ is a quadratic polynomial in poloidal flux ψ and vanishes linearly at the plasma edge. At elongation 2.5, the current limit corresponds to $q_\psi = 2$ for $q_0 < 1.2$ and $q_\psi = 3$ for $1.2 < q_0 < 2$. For elongation 3, the limit is no longer related to integer q_ψ but is a smooth function of q_0. The maximum current increases with δ and decreases with λ. It is remarkably constant when expressed in terms of q_{95}, $q_{95} \geq 3.3$ for q_0 between 1 and 2 and $\lambda = 0$. We note that the current limits are similar for elongations 2.5 and 3. In fact, for $q_0 < 1.2$, the limit is even slightly higher for $\kappa = 2.5$.

While n = 1 stability is favored by high q_ψ or a large internal inductance, the n = 0 (vertical) stability is favored by a low inductance. To illustrate this, we show in Fig. 2 the limits in internal inductance for n = 1 and n = 0 as functions of elongation for a TCV dee and the same type of current profile as in Fig. 1. While these profiles give a large operating window where both n = 0 and 1 are stable for $\kappa = 2$, the window is considerably reduced at

$\kappa = 2.5$ and nonexistent at $\kappa = 3$. We find that at zero beta, the n = 0 stability is almost entirely determined by the internal inductance, while the n = 1 stability is sensitive to the details of the current profile. We have found advantageous results for a class of current profiles with "shoulders" in the outer region of the plasma. An example of such a current profile is shown in Fig. 3a. For $q_0 = 1.05$, this profile remains n = 1 stable for ℓ_i as low as 0.43, while the "standard" profile shown in Fig. 3b gives an ℓ_i-limit of about 0.54. At $\kappa = 3$ and zero pressure, n = 0 stability requires $\ell_i < 0.5$, which can be satisfied for the profile with shoulders but not by the standard profile. (Another way to ensure both n = 0 and n = 1 stability is to raise q_0. This, however, reduces n = 1 the current limit, which is not the case for the profile in Fig. 3a.)

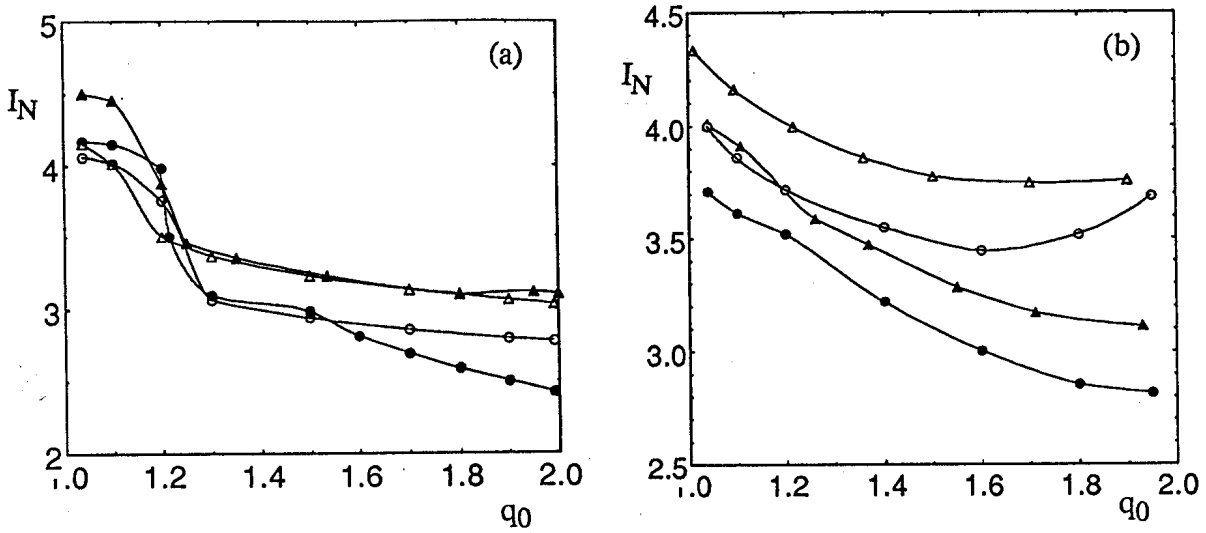

FIGURE 1. Current limit for the n = 1 external kink and different shapes. Circles - $\delta = 0.25$, triangles - $\delta = 0.5$; open symbols - $\lambda = 0$, filled symbols - $\lambda = 0.25$. (a) $\kappa = 2.5$ and (b) $\kappa = 3$.

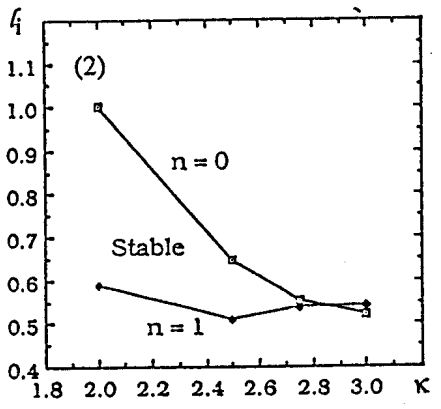

FIGURE 2. Limit in ℓ_i for n = 0 and 1. vs elongation in TCV dee with a simple current profile and $q_0 = 1.05$.

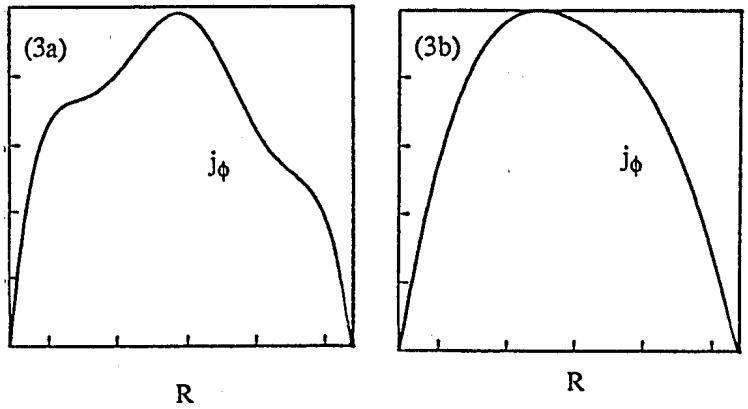

FIGURE 3. (a) Current profile with shoulders and low inductance limit for n = 1. (b) Simple current profile used to generate Fig. 2.

III. BETA LIMITS AT HIGH ELONGATION

III.1 Kink-ballooning limit

Here we present the beta limits imposed by kink and ballooning modes for different shapes (κ = 2, 2.5 and 3; δ = 0.2, 0.5 and 0.8; λ = 0, and 0.2). In this study, the surface averaged toroidal current density I* has been taken as flat in the central region, matched by a cubic polynomial in ψ in the outer region with $I^* = dI^*/d\psi = 0$ at the edge and I* and $dI^*/d\psi$ everywhere continuous. These profiles give rather high internal inductance, which is favorable for n = 1 stability (but makes the n = 0 unstable at high elongation). The normalized current

was fixed at 2.96 for $\kappa = 2.5$ and 3, and $I_N = 2.22$ for $\kappa = 2$.

Figure 4 shows the beta limits imposed by kink and ballooning stability as functions of elongation for different δ and λ. We see that the effects of δ and λ compensate each other and the highest beta limits are obtained for highly triangular plasmas, δ large and λ small. Furthermore, at high triangularity, $\delta = 0.5$ or 0.8, the limit takes the largest values at elongation $\kappa = 2.5$. The best result obtained here is for $\kappa = 2.5$, $\delta = 0.8$ and $\lambda = 0$, where the limit is 8.3%. It may be noted that this shape is close to that of the DIII-D discharge with record β of 11 % [2]. With correction for the inverse dependence on aspect ratio, $\beta = 8.3$ % at $A = 3.7$ corresponds to $\beta = 10.4$ % at $A = 2.96$, which is close to the experimental result.

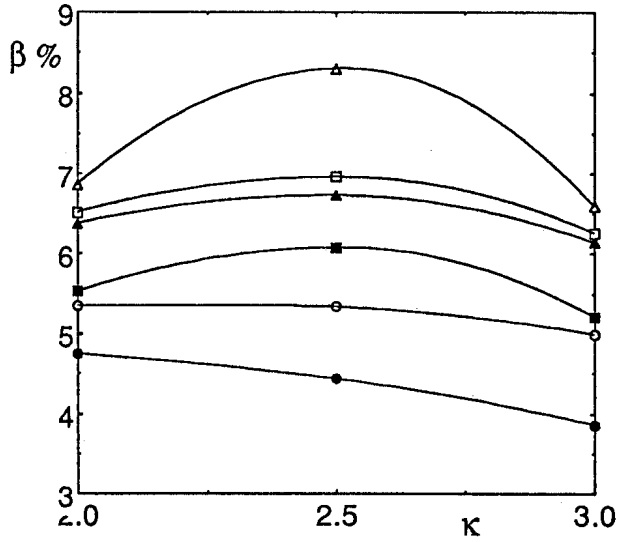

FIGURE 4. Beta limits for kink and ballooning stability and different plasma shapes. Circles - $\delta = 0.2$, squares - $\delta = 0.5$ and triangles - $\delta = 0.8$. Open symbols - $\lambda = 0$, filled - $\lambda = 0.2$.

III.2 Limits imposed by vertical stability

As discussed in Sec. II, an important issue at high elongation is the vertical stability which requires a low internal inductance. Previous studies indicate that the highest beta limits both for kink [2] and ballooning [6] occur for high internal inductance. To examine the effect of the n = 0 stability on the beta limits for TCV, we have considered current profiles with different internal inductance in a TCV dee with $\kappa = 3$. Figure 5 shows the beta limits for ballooning (dotted), n = 1 (solid) and n = 0 (dashed curves) vs. the normalized current for three different sequences of current profiles. In order of decreasing ℓ_i at fixed I_p these are: 1 - standard profile without shoulders and two profiles with 2 - weak and 3 - large shoulders. Figure 6 shows the internal inductance as a function of I_N at the n = 1 limit for these equilibria.

The n = 0 stability is primarily dependent on the internal inductance. Figure 5 shows that pressure has a strong stabilizing effect on the n = 0 mode. The limit in internal inductance increases by about 0.1 when β is increased from 0 to 6 % for these equilibria. (Note that the n = 0 mode is stable for $\beta > \beta_{crit}(I_N)$. For the sequence (1) of equilibria with the highest inductance, the n = 0 mode requires $\beta > 10$ % for stabilization, which is clearly higher than the n = 1 limit, so this sequence is always unstable.) The finite β stabilization appears to be due to an outward shift of the maximum in the current density which redistributes the eddy currents in the wall towards the outboard side. This is strongly stabilizing. Thus, finite pressure widens the class of current profiles stable to both n = 0 and 1 at high elongation. We find that the pressure effect on n = 0 stability is similar at $\kappa = 2.5$.

The n = 1 beta-limit is higher for the cases of higher inductance (curve 1), in agreement with the results of [2]. The two other cases, medium and low ℓ_i (curves 2 and 3) give almost the same values with a maximum of about 4 %. It is clear from Fig. 5 that the equilibrium sequence with the lowest inductance is stable over a fairly large range of plasma current, while

the sequence of intermediate inductance gives a smaller operational window and that of high inductance is always unstable. Figure 5 shows that the ballooning limit is almost independent of the inductance which is different from results for lower elongation reported in [6]. We conclude from Fig. 5 that at $\kappa = 3$, the beta limit is set entirely by the n = 0 and n = 1 modes, the ballooning limit being always higher.

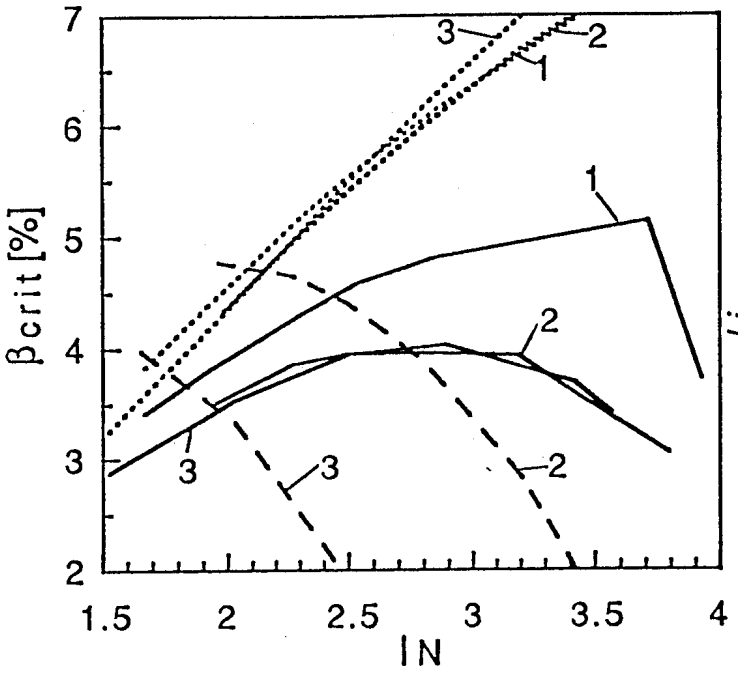

FIGURE 5. Beta limits for ballooning (dotted), n = 0 (dashed) and n = 1 (solid) vs. normalized current for a TCV dee ($\kappa = 3$, A = 3.7) and the equilibrium sequences described in Sec. III.2.

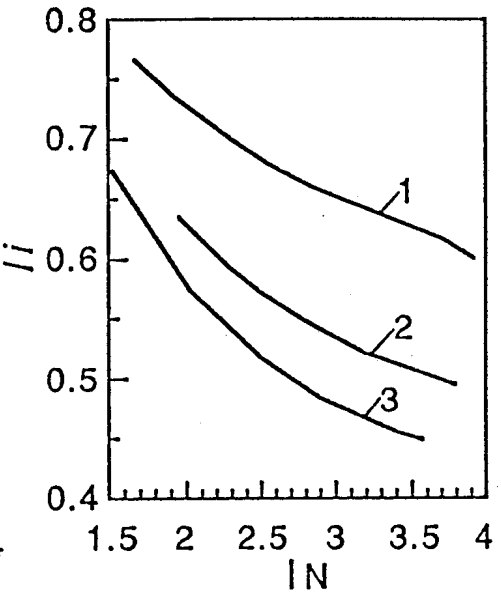

FIGURE 6. Internal inductance vs. normalized plasma current for the same equilibrium sequences as in Figure 5.

IV. CONCLUSION

In conclusion, the beta limit of highly elongated tokamaks increases with triangularity. As a function of elongation, the limit shows a maximum for $\kappa \approx 2.5$. The n = 1 and ballooning limits fall weakly at higher elongation. However, vertical stability for high elongation requires operation at low inductance and this causes a more significant decrease of the n = 1 beta limit. At high elongation, the beta limit is set entirely by n = 0 and n = 1 stability. Finite pressure is clearly favorable for vertical stability at high elongation.

Acknowledgement: This research was funded in part by the Swiss National Science Foundation.

References

[1] TROYON, F., et al., Plasma Phys. Controlled Fusion **26** (1984) 209.
[2] LAZARUS, E.A., et al., Phys. Fluids **B3** (1991) 2220.
[3] LÜTJENS, H., BONDESON, A., ROY, A., Comp. Phys. Comm. **69** (1992) 287.
[4] WARD, D.J., JARDIN, S.J., to appear in Nucl. Fusion **32**, 1992.
[5] BONDESON, A., VLAD, G., LÜTJENS, H., to appear in Phys. Fluids **B4**, 1992.
[6] LAO, L.L., et al., Phys. Fluids **B4** (1992) 232.

*On leave from Uppsala University, Sweden

ANISOTROPIC PRESSURE NUMERICAL 3D MHD EQUILIBRIA

S. P. Hirshman*, **W. A. Cooper**, S. Merazzi†, R. Gruber‡
Centre de Recherches en Physique des Plasmas,
Association Euratom-Confédération Suisse,
Ecole Polytechnique Fédérale de Lausanne,
Lausanne, Switzerland

We introduce the energy functional

$$W \equiv \int\int\int d^3x \Big[\frac{B^2}{2\mu_0} + \frac{p_{\|}}{\Gamma - 1}\Big], \tag{1}$$

and demonstrate that its minimisation can be used to determine three dimensional (3D) magnetohydrodynamic (MHD) equilibria with anisotropic pressure. We express the parallel pressure as

$$p_{\|}(s,B) = M(s)[\Phi'(s)]^{\Gamma} \frac{1 + p(s,B)}{\Big\langle 1 + p(s,B)\Big\rangle^{\Gamma}}, \tag{2}$$

where $M(s)$ is the plasma mass function, $\Phi(s)$ is the toroidal magnetic flux function, Γ is the adiabatic index and $p(s,B)$ is the function that controls the anisotropy in the pressure. We constrain the poloidal magnetic flux function Ψ to be a flux surface quantity, thus the magnetic flux surfaces remain nested. We introduce a coordinate system (s,u,v) where s labels the magnetic flux surfaces, u is the periodic poloidal angle variable and v is the geometric toroidal angle. We then vary W with respect to an artificial time parameter t in such a manner that the plasma mass function, the magnetic flux functions and the coordinates s, u and v remain invariant. The energy functional acquires the form

$$\begin{aligned}\frac{dW}{dt} = &-\int\int\int dsdudvF_R\frac{\partial R}{\partial t} - \int\int\int dsdudvF_Z\frac{\partial Z}{\partial t} \\ &-\int\int\int dsdudvF_\lambda\frac{\partial \lambda}{\partial t} \\ &-\int\int_{s=1} R\Big(p_\perp + \frac{B^2}{2\mu_0}\Big)\Big(\frac{\partial R}{\partial u}\frac{\partial Z}{\partial t} - \frac{\partial Z}{\partial u}\frac{\partial R}{\partial t}\Big).\end{aligned} \tag{3}$$

The distance from the major axis is R and the distance from the horizontal midplane is Z. The function λ is a periodic stream function that iteratively renormalises the poloidal angle to minimise the spectral width that is required to describe the MHD equilibrium state [1]. The perpendicular pressure is $p_\perp$. The last term constitutes the deformation of the plasma-vacuum interface boundary that vanishes by definition for fixed boundary calculations. The coefficients F_R and F_Z correspond to the cylindrical MHD force components $F_R = \sqrt{g}R\nabla v\times\nabla Z\cdot\mathbf{F}$ and $F_Z = \sqrt{g}R\nabla R\times\nabla v\cdot\mathbf{F}$, respectively, where

$$\mathbf{F} = -\nabla\Big(p_\perp + \frac{B^2}{2\mu_0}\Big) + (\mathbf{B}\cdot\nabla)(\sigma\mathbf{B}). \tag{4}$$

These can be written as

$$\begin{aligned} F_R = {} & \frac{\partial}{\partial u}\big[\sigma\sqrt{g}B^u(\mathbf{B}\cdot\nabla R)\big] + \frac{\partial}{\partial v}\big[\sigma\sqrt{g}B^v(\mathbf{B}\cdot\nabla R)\big] \\ & -\frac{\partial}{\partial u}\big[R\frac{\partial Z}{\partial s}\big(p_\perp + \frac{B^2}{2\mu_0}\big)\big] + \frac{\partial}{\partial s}\big[R\frac{\partial Z}{\partial u}\big(p_\perp + \frac{B^2}{2\mu_0}\big)\big] \\ & +\frac{\sqrt{g}}{R}\big[\big(p_\perp + \frac{B^2}{2\mu_0}\big) - \sigma R^2(B^v)^2\big], \end{aligned} \tag{5}$$

$$\begin{aligned} F_Z = {} & \frac{\partial}{\partial u}\big[\sigma\sqrt{g}B^u(\mathbf{B}\cdot\nabla Z)\big] + \frac{\partial}{\partial v}\big[\sigma\sqrt{g}B^v(\mathbf{B}\cdot\nabla Z)\big] \\ & +\frac{\partial}{\partial u}\big[R\frac{\partial R}{\partial s}\big(p_\perp + \frac{B^2}{2\mu_0}\big)\big] - \frac{\partial}{\partial s}\big[R\frac{\partial R}{\partial u}\big(p_\perp + \frac{B^2}{2\mu_0}\big)\big], \end{aligned} \tag{6}$$

where B^u and B^v are the poloidal and toroidal components of the magnetic field in the contravariant representation. The effective plasma current density field is defined as $\mathbf{K} = \nabla\times(\sigma\mathbf{B})$, where $\sigma > 0$ is the firehose stability parameter that characterises plasmas with anisotropic pressure [2]. The vanishing of F_λ corresponds to the condition that $\mathbf{K}\cdot\nabla s = 0$, which implies that the effective current density lines lie on flux surfaces. To diagnose the quality and accuracy of a 3D equilibrium state computed through the simultaneous minimisations of F_R, F_Z and F_λ, it is useful to evaluate the flux surface average of the radial MHD force balance relation given by

$$\mathbf{F} = -\frac{\partial p_{||}}{\partial s}\bigg|_B \nabla s + \mathbf{K}\times\mathbf{B}. \tag{7}$$

The vanishing of this equation constitutes a form of the 3D Grad-Schlüter-Shafranov equation.

This formulation of the 3D anisotropic pressure MHD equilibrium problem lends itself to an easy adaptation of the techniques that resulted in the development of the preconditioned VMEC code for scalar pressure equilibria [3]. The internal MHD forces and the preconditioning algorithm that is designed to improve the convergence properties of the steepest descent energy minimisation method utilised in VMEC have been appropriately modified to treat the condition $p_{||} \neq p_\perp$. A more detailed description of the derivation will appear elsewhere [4].

As an application, we consider a fixed boundary calculation in an ATF torsatron configuration [5]. To model an energetic trapped particle layer induced by radio frequency heating or neutral beam injection, we choose the factor $p(s,B)$ as

$$p(s,B) = p_h(s)\bigg[\frac{B_{min}(s)}{B}\bigg]^8, \tag{8}$$

with $p_h(s) = p_c s^3(1-s)^2$. The hot particle pressure thus vanishes both at the origin

and at the edge. The radial variable s is proportional to the volume enclosed. The plasma mass function required to compute the thermal component is chosen as $M(s) = M(0)(1-s)^2$ and the effective toroidal plasma current is prescribed to vanish within each flux surface. We consider two cases in which the peak β value due to the energetic species remains fixed at 4.83%. The perpendicular (parallel) pressure component contributes 2/3 (1/3) to the β values we quote here. Choosing $M(0) = 0.4$ and $p_c = 120$, we obtain an equilibrium in which the total $\beta = 0.55\%$, the thermal $\beta = 0.16\%$ and the perpendicular hot particle $\beta = 0.55\%$. Choosing $M(0) = 3.67$ and $p_c = 12$, we obtain an equilibrium in which the total $\beta = 1.79\%$, the thermal $\beta = 1.52\%$ and the perpendicular hot particle $\beta = 0.38\%$. The rotational transform profiles for these cases are shown in Fig. 1 and the differential volume $dV/d\Phi$ profiles are shown in Fig. 2. In the low β case, the hot particle pressure induces a weak magnetic well region in the middle third of the plasma volume. At moderate β, the thermal pressure gradient digs a magnetic well in the centre of the plasma.

Acknowledgements

This work was sponsored in part by the Ecole Polytechnique Fédérale de Lausanne, by the Fonds National Suisse pour la Recherche Scientifique, by Euratom and by the Office of Fusion Energy, United States Department of Energy, under Contract No. DE-AC05-84OR21400 with Martin Marietta Energy Systems, Inc.

*ORNL, Oak Ridge, Tennessee, USA; †IMHEF/EPFL, Lausanne, Switzerland; ‡GASS/CSCS, Manno, Switzerland.

References

[1] S. P. Hirshman and J. C. Whitson, *Phys. Fluids* **26** (1983) 3553.

[2] H. Grad, in *Magneto – Fluid and Plasma Dynamics*, *Symposia in Applied Mathematics* (American Mathematical Society) **18** (1967) 162.

[3] S. P. Hirshman and O. Betancourt, *J. Comput. Phys.* **96** (1991) 99.

[4] W. A. Cooper, S. P. Hirshman, S. Merazzi and R. Gruber, *Comput. Phys. Commun.* (to be published).

[5] M. Murakami, B. A. Carreras, L. R. Baylor, G. L. Bell, T. S. Bigelow, A. C. England, J. C. Glowienka, H. C. Howe, T. C. Jernigan, D. K. Lee, V. E. Lynch, C. H. Ma, D. A. Rasmussen, J. S. Tolliver, M. R. Wade, J. B. Wilgen and W. R. Wing, *Phys. Rev. Lett.* **66** (1991) 707.

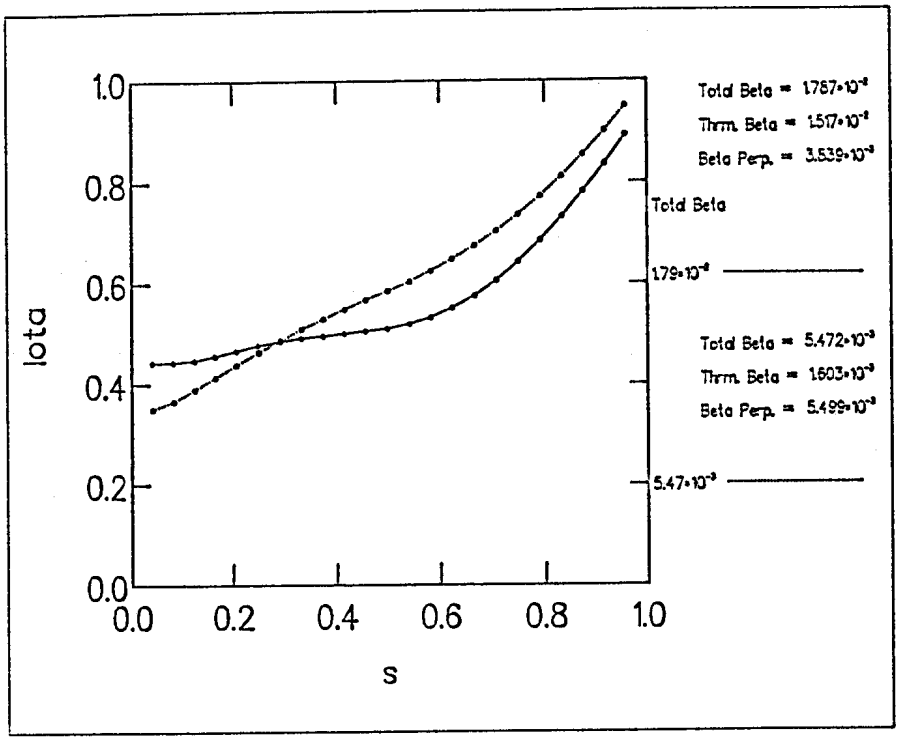

Figure 1: The rotational transform profile in an ATF configuration for cases with total $\beta = 1.79\%$ and total $\beta = 0.55\%$ with fixed peak hot $\beta = 4.83\%$.

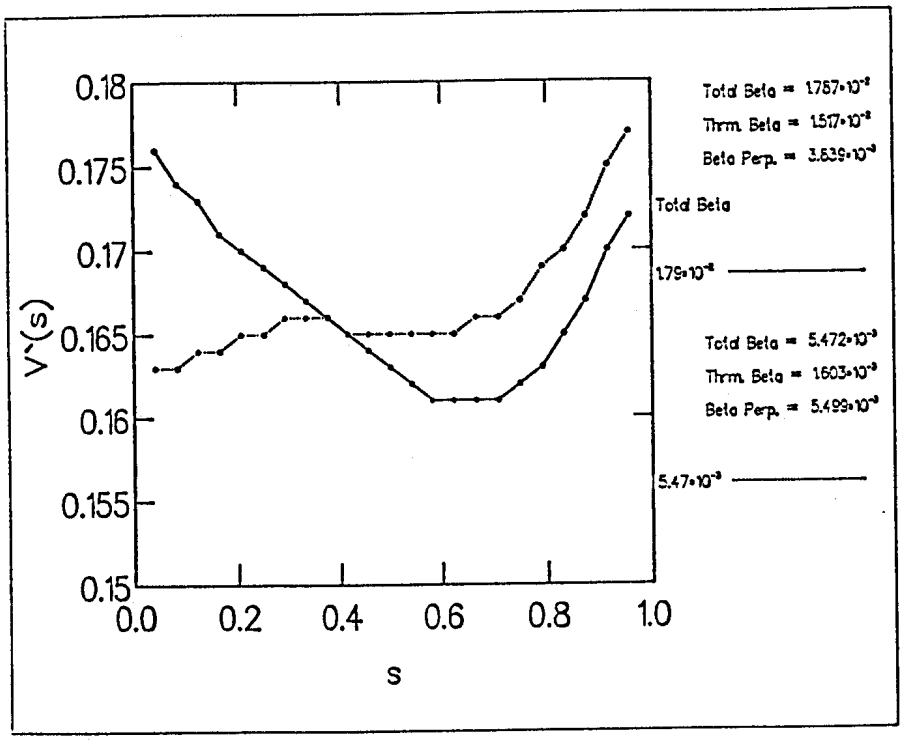

Figure 2: The differential volume profile in an ATF configuration for cases with total $\beta = 1.79\%$ and total $\beta = 0.55\%$ with fixed peak hot $\beta = 4.83\%$.

LINEAR MHD STABILITY COMPUTATIONS IN 3D PLASMAS

W. A. Cooper, Y. Nakamura*, M. Wakatani*, R. Gruber†, S. Merazzi‡, D. V. Anderson◇ and U. Schwenn*
Centre de Recherches en Physique des Plasmas,
Association Euratom-Confédération Suisse,
Ecole Polytechnique Fédérale de Lausanne,
Lausanne, Switzerland

The equations that govern the global and local magnetohydrodynamic (MHD) stability properties of three dimensional (3D) plasma confinement configurations constrained to have nested magnetic flux surfaces with a noninteracting hot electron species are presented. In the absence of hot particles, the model reduces to the ideal MHD limit. Specific applications presented here will concentrate on the 10 field period LHD torsatron device and toroidal ripple effects in the JET Tokamak within the ideal MHD model. Applications to problems in which an energetic species plays an important role will be deferred to future work.

The energy principle within a plasma with a noninteracting hot electron current layer can be written as [1,2]

$$\delta W_p = \frac{1}{2}\int\int\int d^3x \left[C^2 + \Gamma p|\nabla\cdot\xi|^2 - D|\xi\cdot\nabla s|^2\right], \tag{1}$$

where the vector $\mathbf{C}$ corresponds to a modified perturbed magnetic field, the second term describes the compressibility of the plasma, D constitutes the MHD instability driving term, ξ is the perturbed displacement vector and s is the radial variable the labels the magnetic flux surfaces. We introduce a modified Boozer magnetic coordinate system [3] (s,θ,ϕ) applicable to plasmas with anisotropic pressure and expand the perturbation as

$$\xi = \sqrt{g}\xi^s\nabla\theta\times\nabla\phi + \eta\frac{\mathbf{B}\times\nabla s}{B^2} + \left[\frac{J(s)}{\Phi'(s)\sigma B^2}\eta - \mu\right]\mathbf{B}, \tag{2}$$

where $\sqrt{g}$ is the Jacobian, σ is the firehose stability parameter of anisotropic plasmas [4], $\Phi(s)$ is the equilibrium toroidal magnetic flux function and $J(s)$ is the effective toroidal plasma current function determined from $\mathbf{K} = \nabla\times(\sigma\mathbf{B})$. The components of the perturbation are $\xi^s = \xi\cdot\nabla s$, η and μ. The perturbed magnetic energy contribution is decomposed as $\sqrt{g}C^2 = \sqrt{g}C^sC_s + \sqrt{g}C^\theta C_\theta + \sqrt{g}C^\phi C_\phi$, where the the components in the contravariant representation are

$$\sqrt{g}C^s = \sqrt{g}\mathbf{B}\cdot\nabla\xi^s = \left[\Psi'(s)\frac{\partial\xi^s}{\partial\theta} + \Phi'(s)\frac{\partial\xi^s}{\partial\phi}\right], \tag{3}$$

$$\sqrt{g}C^\theta = \frac{\partial\eta}{\partial\phi} - \Psi'(s)\frac{\partial\xi^s}{\partial s} - \frac{1}{\sigma B^2}\left[\sigma B^2\Psi''(s) + \frac{I(s)\mathbf{j_p}\cdot\mathbf{B}}{|\nabla s|^2} + \sigma p'(s)\Psi'(s)\right], \tag{4}$$

$$\sqrt{g}C^\phi = -\frac{\partial\eta}{\partial\theta} - \Phi'(s)\frac{\partial\xi^s}{\partial s} - \frac{1}{\sigma B^2}\left[\sigma B^2\Phi''(s) + \frac{J(s)\mathbf{j_p}\cdot\mathbf{B}}{|\nabla s|^2} + \sigma p'(s)\Phi'(s)\right]. \tag{5}$$

The poloidal magnetic flux and effective current flux functions are denoted by $\Psi(s)$ and $I(s)$, respectively. The prime denotes a derivative with respect to s. The components of

in LHD are fully internal in nature, vanishing close to the plasma-vacuum interface even when the conducting wall is placed at a great distance. The Mercier stability indicates a first unstable domain bounded by $0.5\% \leq \beta \leq 2.2\%$. A second Mercier unstable domain that encompasses the region where the magnetic shear vanishes in this torsatron device is triggered at $\beta > 3.6\%$. The *stable* domain between the two unstable regions is not actually fully stable. Mercier instability persists but only very locally about resonant surfaces with rational rotational transform values within one period ($\iota_p = 1/18$, $1/17$, $1/16$, $1/15$, etc). It could be argued, however, that local flattening of the pressure profile about these surfaces would render stability without altering significantly the β value that could be achieved. Localised ballooning modes become unstable at $\beta = 1.5\%$ and remain unstable to $\beta > 5\%$ without any indication of second stability. The dominant ballooning structures are localised about magnetic field lines that cross the outer edge of the prolate up-down symmetric cross section. The ballooning modes on the more conventional field lines that cross the outer edge of the oblate up-down symmetric cross section become unstable when $\beta > 3.7\%$ and impose the inner stability boundary at $\beta > 4\%$ in Fig. 1. The large variation of ballooning stability from field line to field line calls into question the applicability of ballooning stability predictions based on the stellarator expansion method. The poloidal field design in the LHD device permits a significant enhancement of the magnetic well through an outward shift of the magnetic axis. The magnetic well can play a big impact in the stabilisation of localised pressure driven modes to improve the predictions of the 3D ideal MHD model that we present here. On the other hand, the outward axis shift deteriorates particle confinement and erodes the quality of the outer magnetic flux surfaces. The flexibility of the LHD device should allow a quantitative experimental evaluation ot the tradeoff between MHD stability versus particle confinement and flux surface fragility to determine the optimal operational conditions in torsatrons.

The effects of toroidal field ripple on ideal MHD ballooning stability in JET are investigated with a simplified model in which the toroidal coils are infinitely elliptical [8]. Selfconsistent 3D MHD equilibria are calculated with the VMEC code [9]. The pressure profile is bell-shaped to model the H-mode and the toroidal current profile is prescribed as rounded box-like in shape. The magnitude of the ripple depends on the coil discreteness and on the gap between the coils and the plasma. The critical β value as a function of the inverse number of coils is shown in Fig. 2 for cases in which the plasma-coil gap is 20, 30, 40 and 50 *cm*. With 32 coils, the β value is virtually unaltered when the coil plasma distance exceeds 30 *cm*. With 16 coils, the critical β degrades when the gap is smaller than 40 *cm*.

*Kyoto Univ., Japan; †GASS/CSCS, Manno, Switzerland. ‡IMHEF/EPFL, Lausanne, Switzerland; °NERSC/LLNL, Livermore, USA; *MPIPP, Garching, FRG.

REFERENCES

[1] J. L. Johnson, R. M. Kulsrud and K. E. Weimer, *Plasma Phys.* **11** (1969) 463.
[2] D. B. Nelson and C. L. Hedrick, *Nucl. Fusion* **19** (1979) 285.
[3] A. H. Boozer, *Physics Fluids* **23** (1980) 904.
[4] H. Grad, in *Magneto – Fluid and Plasma Dynamics, Symposia in Applied Mathematics* (American Mathematical Society) **18** (1967) 162.
[5] D. V. Anderson, W. A. Cooper, R. Gruber, S. Merazzi and U. Schwenn, *Int. J. Supercomp. Appl.* **4** (1990) 34.
[6] R. L. Dewar and A. H. Glasser, *Physics Fluids* **26** (1983) 3038.
[7] W. A. Cooper, *Plasma Phys. Contr. Fusion* (1992) in press.
[8] J. L. Johnson and A. H. Reiman, *Nucl. Fusion* **28** (1988) 1116.
[9] S. P. Hirshman and O. Betancourt, *J. Comput. Phys.* **96** (1991) 99.

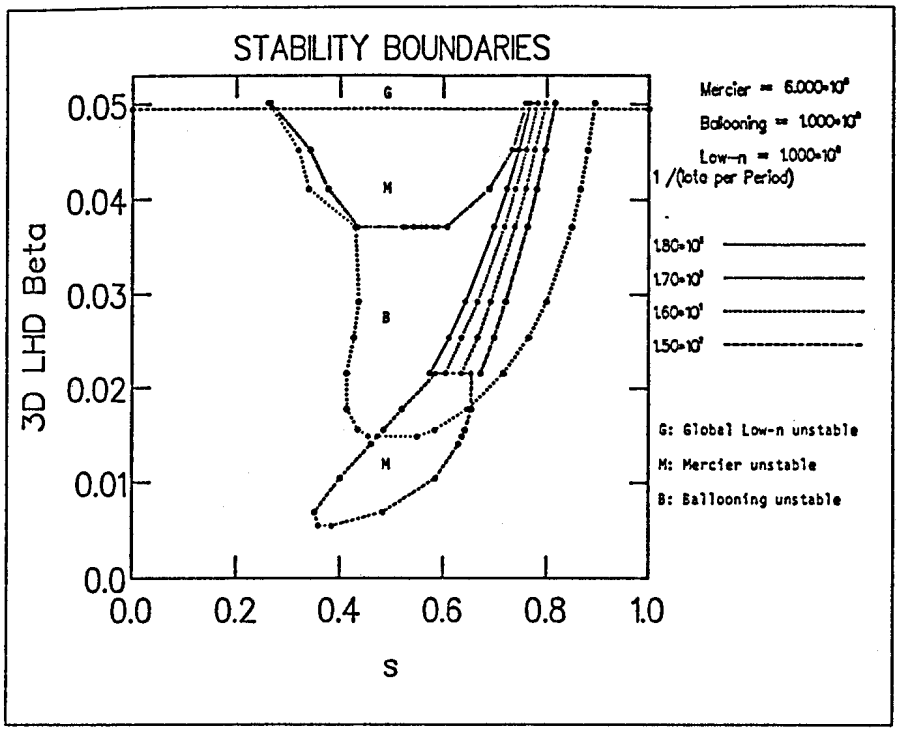

Figure 1: The MHD stability boundaries in the LHD torsatron imposed by global low n modes, Mercier modes and ballooning modes.

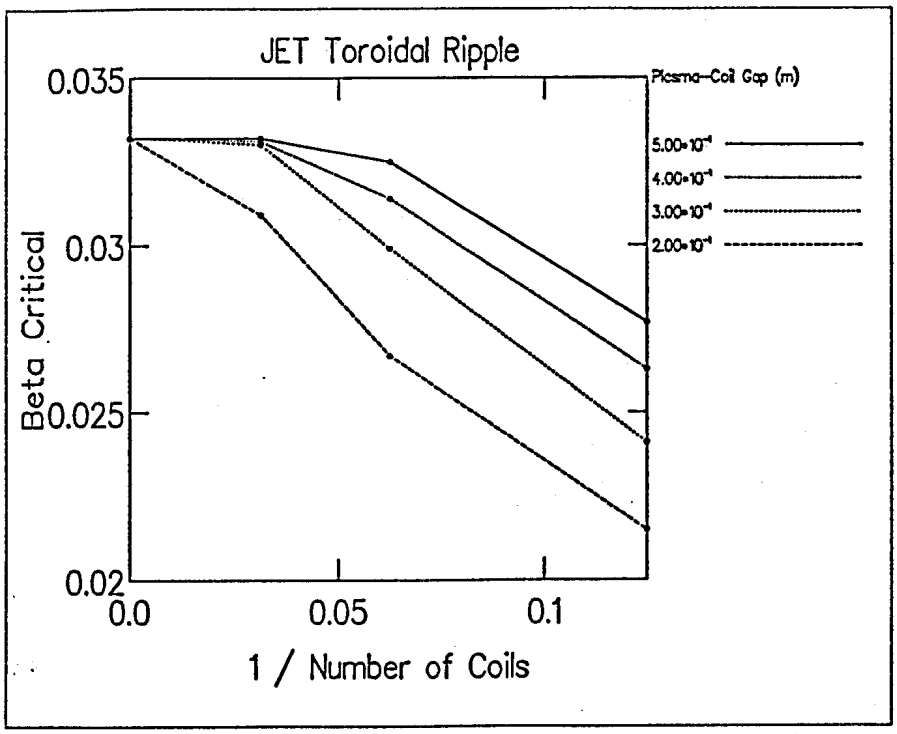

Figure 2: The β limit imposed by ballooning instabilities versus the inverse number of toroidal coils in JET for plasma-coil gaps of 50, 40, 30 and 20 cm.

Observation of two wave induced chaos in a magnetized plasma

A.Fasoli, P.J.Paris, M.Q.Tran, and F.Skiff[+]

Centre de Recherches en Physique des Plasmas, Association Euratom-Confédération Suisse,
Ecole Polytechnique Fédérale de Lausanne, CH-1007 Lausanne, Switzerland

Introduction

The problem of wave induced stochasticity in plasmas is being studied extensively because of its general interest in chaotic dynamics and of its possible direct consequences in space and laboratory plasmas, such as anomalous transport and non-linear heating and particle acceleration [1].

Several theoretical investigations have been performed in the recent past, based mainly on hamiltonian single particle models, which predict the transition to stochasticity in terms of the wave amplitude and spectrum [2]. The majority of these theories are non self-consistent, that is, do not take into account possible mutual interactions between wave and particles. Self-consistency characterizes actual experiments, in which non-linear wave-wave interactions, in the case of several modes in the plasma, are also naturally present.

It has been shown theoretically and experimentally [3,4], that in a magnetized plasma a wave propagating at a finite angle with respect to the B-field can generate chaos in particle orbits and, consequently, fast ion heating.

The case of two (or more) waves propagating at different phase velocities is predicted to be more efficient for the heating: the threshold amplitude for the occurrence of chaos should be lower, due to a large number of resonances in phase space.

In our experiment we investigate the interaction between ions and two propagating electrostatic modes in a Q-machine plasma.

In particular, our aim is to perform and integrate observations of the collective ion response (wave characteristics), of ion kinetic features (modification of the distribution functions, time scale for heating) and of single particle orbit modifications (phase space transport).

Experimental set-up and diagnostics apparatus

The experiments are performed on the LMP barium Q-machine [5], a uniformly magnetized plasma column characterized by ion and electron temperatures of the order of 0.2 eV and densities in the range of 10^8-10^{10} cm^{-3}. The maximum axial B-field is 0.3 T ($f_{ci} \cong 30$ kHz). Sheath acceleration at the hot plate causes a supersonic ion drift $v_D \approx 10^5$ cm/s. Low degrees of spatial and temporal variations and fluctuations can be achieved in current operation (e.g. $\delta n/n < 1\%$).

Electrostatic ion waves ($f \approx f_{ci}$) are launched by a capacitive antenna consisting of 4 rings placed directly around the plasma column at variable relative distances and phase.

The diagnostic system is based on the technique of Laser Induced Fluorescence (LIF) [6], which provides a direct measurement of ion distributions with good spatial and temporal resolution (the latter allows time resolved measurements of f(v) and synchronous detection for $f^1(v)$).

LIF can be extended to an optical tagging method, based on the spin polarization of ground state ions [7]: sets of test-ions can thus be created and followed in their evolution in order to infer the nature of particle orbits. A schematic of the LMP machine, including the electrostatic antenna and the geometry for the LIF laser beam injection and detection systems, is shown in fig.1.

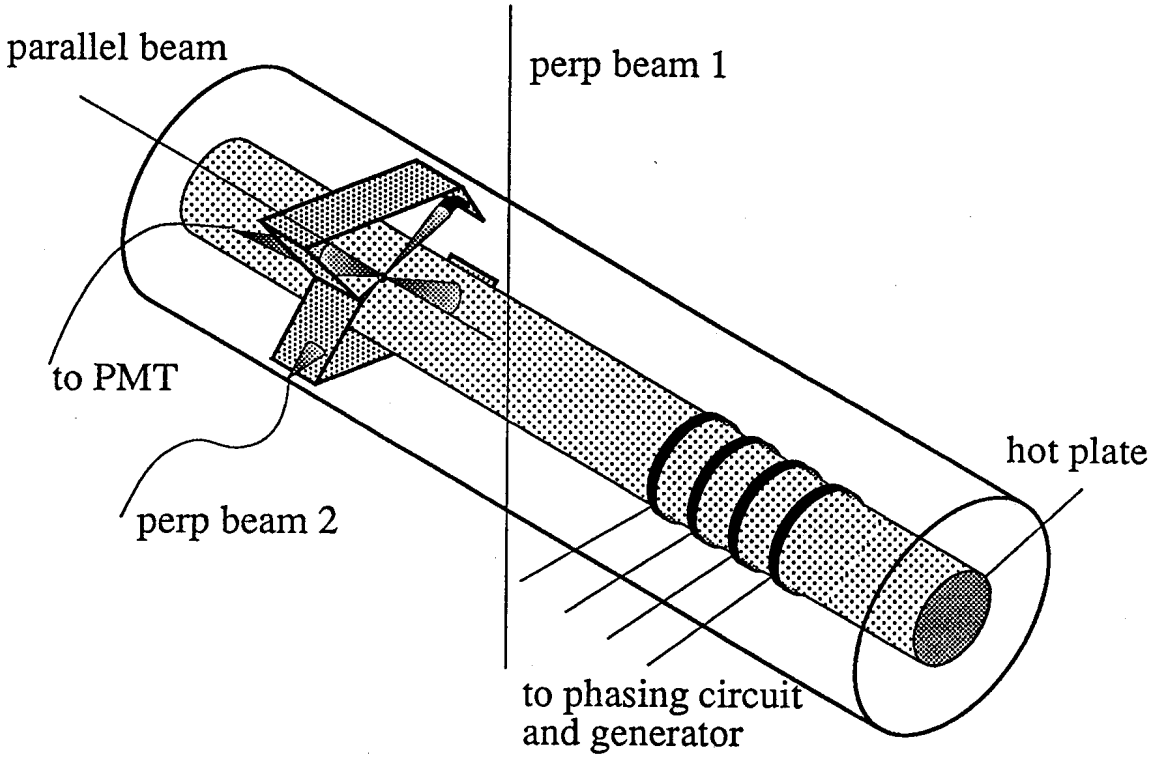

Fig.1: LMP experimental arrangement

Results and discussion

The wave spectrum excited by the 4 ring antenna in the plasma at one frequency f ($f_{ci}<f<2f_{ci}$) is composed in the parallel plane by two modes with two different phase velocities, and in the perpendicular plane by the two branches (forward and backward) of the ESICW dispersion relation [8]. In fig.2 we see the $k_{||}$ spectrum at 25 kHz ($f\approx1.1f_{ci}$), as directly evinced from the observed form of the first order perturbed distribution function. Two distinct peaks are clearly visible, corresponding to the two phase velocities $v_{\phi}1$, $v_{\phi}2$.($\Delta v_{\phi}\approx5\ 10^4$ cm/s).

The difference Δv_{ϕ} is such that on the parallel ion phase space one can consider, to a first approximation, only primary resonances and neglect the multiple island structure introduced by the non zero perpendicular wavenumber (natural cyclotron resonances should appear, spaced by $2\pi f_{ci}$; it is indeed their interaction which generates chaos in the one wave case).

The hamiltonian models predict therefore a transition to a stochastic regime when the wave amplitude is such that the two resonances start to overlap. A stochasticity parameter can be introduced: $K = 2\ (A_1^{1/2} + A_2^{1/2})$, where $A_i=e\phi_i/m(\Delta v_{\phi})^2$ is the amplitude of the mode i (i=1,2). K=1 is the threshold for the transition, in the frame of the single particle theory; in macroscopic terms, K>1 should imply a fast ion heating.

In fig.3 we plot the parallel and perpendicular ion temperatures as functions of the excitation amplitude. We notice that a threshold value exists, above which a significant heating occurs. A calibration of the wave amplitude through the ion dielectric response [9] allows us to compare the observed threshold to the theoretical prediction for the experimental wave parameters. K=1 corresponds to the shaded region on the amplitude axis of the graph. We see that, inside the error bar, mainly due to the wave amplitude calibration procedure, experiment and single particle theory agree.

By pulsing the wave excitation generator, and observing the time resolved ion distribution from the time t=0 (when the RF is started) onwards, an accurate estimation of the heating time can be achieved. More specifically, by plotting the increase in the ion temperature (or mean square ion velocity) vs. the time, if the dependence is linear, a direct estimation of the velocity space diffusion coefficient can be obtained. This is shown in fig. 4, for the case of 25 kHz and just above threshold. The resulting v-space diffusion coefficient is more than one order of magnitude larger than the collisional coefficient.

The mechanism responsible for the heating, therefore, is independent of collisional processes and can be attributed to a transition to chaos in particle trajectories. An additional proof of this mechanism comes from the tag measurements, which evidentiate an exponential separation in time of initially close ion orbits, both in velocity space and in real space.

At frequencies for which only one mode in parallel can be excited in the plasma, no heating is observed, up to amplitudes where secular perturbations of the antenna and intrinsic non-linearities (e.g. harmonic generation) become effective. The case of two waves is then experimentally demonstrated to be more favorable in the achievement of chaos and stochastic heating.

By further increasing the amplitude of the wave(s) well above threshold, another regime is observed: heating no longer takes place, and no more than one mode seems to be excited in the plasma. On the other hand, in the pulsed regime, by following time evolution further on after the heating is reached, temperature is observed to decrease and eventually to return to its unperturbed value (or even lower).

The two results can be interpreted as a manifestation of the feed-back action of the particles on the waves. In fact, the ion orbits undergo a transition in their topology, from regular to chaotic: the plasma oscillating fields, which are issued from collective motions of the charged particles and therefore are derived explicitly from integration of the particle trajectories, are necessarily modified. In particular, experimental observations close to the threshold for the transition to the chaotic regime seem to indicate that of the two modes only one survives. The conditions for the occurrence of chaos are then no longer satisfied, and the plasma tends to relax to its unperturbed equilibrium.

Conclusions

Stochasticity in ion dynamics originated by the interaction between particles and two electrostatic propagating plasma waves has been observed in a magnetized plasma. Optical measurements at different scales, from the single particle to the macroscopic, allowed a determination of the wave features, the kinetic ion response and the plasma heating mechanism.

Chaos appears to be limited by self-consistent effects. More results on these effects, as well as the modification of ion transport in the presence of the two waves will be discussed at the presentation.

This work was partially supported by the *Fonds National pour la Recherche Scientifique.*

+Laboratory for Plasma Research, Univ. of Maryland-College Park, USA.

References

[1]See for instance "Intrinsic Stochasticity in Plasmas", edited by G.Laval and D.Grésillon, Editions de Physique, Orsay 1979.
[2]D.F.Escande, *Phys. Rep.* **121**, 166 (1985).
[3]G.R.Smith and A.N.Kaufman, *Phys. Rev. Lett.* **34**, 1613 (1975).
[4]F.Skiff, F.Anderegg and M.Q.Tran, *Phys. Rev. Lett.* **58**, 1433 (1987).
[5]P.J.Paris and N.Rynn, *Rev. Sci. Instrum.* **61**, 1096 (1990).
[6]R.A.Stern, D.N.Hill and N.Rynn, *Phys. Rev. Lett.* **37**, 833 (1981).
[7]F.Skiff et al., *Phys. Lett. A*, **137**, 57 (1989).
[8]T.N.Good et al., *17th EPS Conf. on Controlled Fusion and Plasma Heating*, Amsterdam 1990, part IV, p.1811.

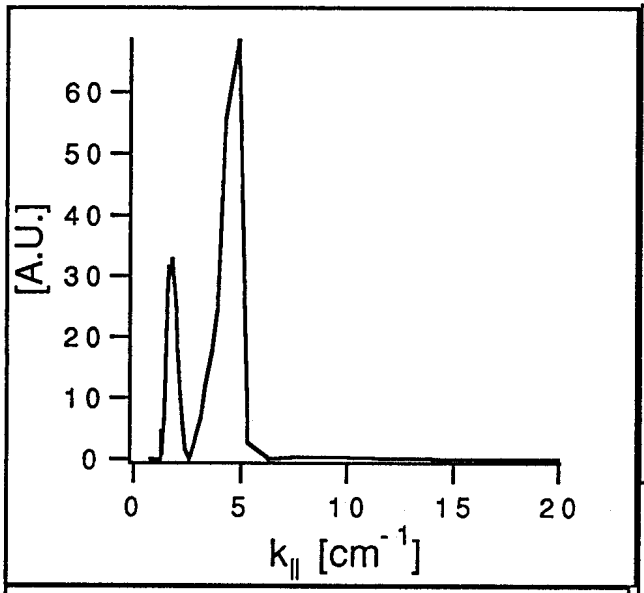

Fig.2: $k_{\|}$ spectrum of the wave electric field at f=25 kHZ, deduced from $f^1(v_{\|})$ via a 1-D Vlasov model

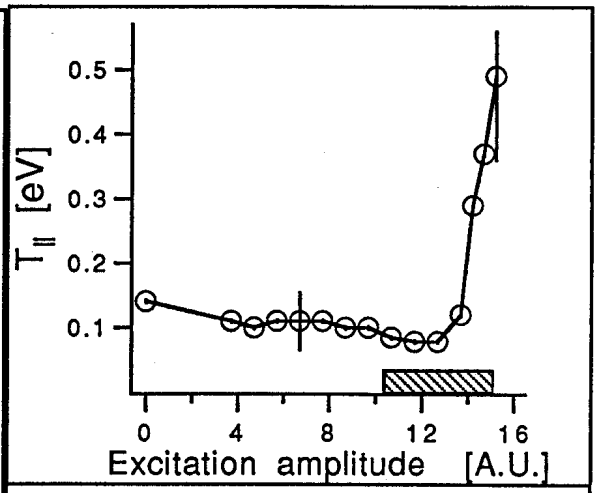

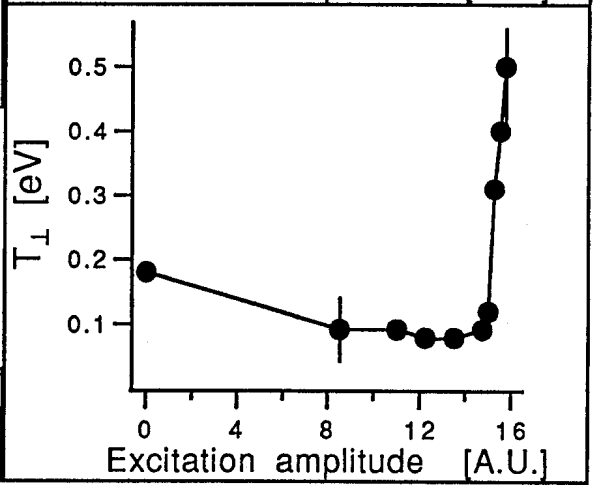

Fig.3: Parallel (top) and perpendicular (bottom) ion temperatures vs. the wave amplitude. The shaded region corresponds to K≅1.

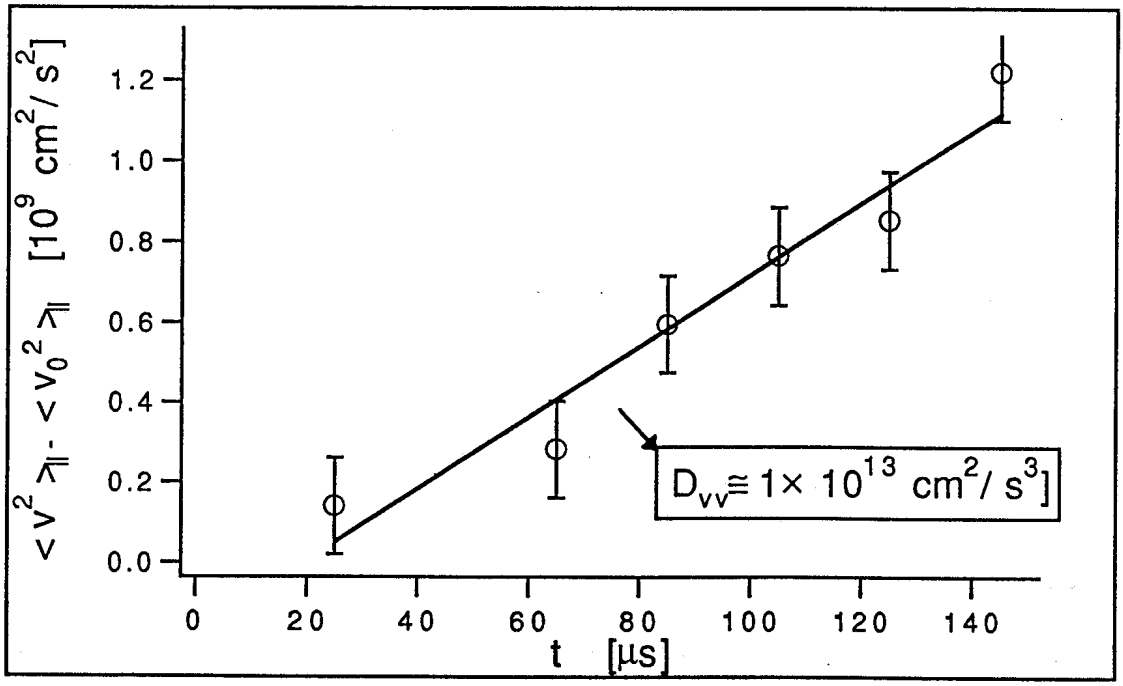

Fig.4: Temporal evolution of the increase of the mean square parallel ion velocity; the RF burst starts at t=0. f=25 kHz; exc. ampl.=15 A.U..

NONLINEAR MECHANISM FOR THE SUPPRESSION OF ERROR FIELD MAGNETIC ISLANDS BY PLASMA FLOW

R.D. Parker

Centre de Recherches en Physique des Plasmas, Association Euratom-Conféderation Suisse, Ecole Polytechnique Fédérale de Lausanne
21 Av. des Bains, CH-1007 Lausanne, Switzerland

Introduction

Non-axisymmetric magnetic field perturbations generated, for example, by errors in the alignment of the field coils are known to lead to reduced confinement in a tokamak,e.g.[1,2]. By inducing the formation of small, stationary, magnetic islands on all rational surfaces they can enhance radial transport and under certain circumstances interact with MHD instabilities to trigger the onset of locked modes[1,2] leading, in some cases, to a disruption of the plasma discharge.

Given the stationary nature of the error field islands it is natural to consider whether they can be reduced significantly by the viscous drag of a sheared flow resulting from a bulk rotation of the plasma. In this paper, we examine this interaction by modelling the nonlinear growth and saturation of force-reconnected magnetic islands driven by a corrugated boundary in a slab plasma with an initially uniform flow. A systematic parameter study is made of the time asymptotic steady state revealing a transition to a *"suppressed state"* as a function of the flow velocity, which becomes discontinuous for sufficiently small viscosity. As such, a critical velocity, V_c, is defined and its dependence on: corrugation amplitude, δW (which is proportional to the error field amplitude, δB), viscosity, ν, and resistivity, $\eta = 1/S$,(S is the Lundquist no.), are delineated. Other parameters to be explored include the wall separation, X_w, and the wavenumber of the perturbation, k_p.

This study follows on from a preliminary numerical investigation[3,4] in which the flow suppression mechanism was first demonstrated. From the nonlinear simulations in the present study a simple intuitive model of the process based on the induced velocity shear,V' and the resistive layer width, Δ_η has been developed. This predicts a scaling for the critical velocity as: $V_c \propto \delta B\, S^{-2/5}\, \nu^{-2/3}$ in good agreement with numerically determined values of V_c ,although the scaling with viscosity diverges toward small ν. The reasons for this divergence are discussed in the light of changes occuring in the flow structure in the limits $\nu >> \eta$ and $\nu << \eta$.The scaling does not appear to be predicted by an alternative, analytical treatment of the phenomenon[5].

Besides the flow suppression mechanism, a variety of fascinating nonlinear phenomena were observed in different regions of the parameter space such as: flow amplified islands, flow induced secondary reconnection and hysteresis. These are discussed in the last section.

To investigate the mechanism of mode-locking it is also necessary to include the interaction of internally as well as externally driven reconnection processes in the presence of flow. This is the subject of the next stage in this study although preliminary simulations with a tearing unstable plasma have already demonstrated cases of full and partial mode-locking[4].

Numerical Model

The basic numerical model adopted is that of a 2-D, plane-slab plasma sandwiched between two, perfectly-conducting walls (at $x = \pm X_w$) with periodic boundary conditions in the y-direction (of periodicity length L_p). An approximately sinusoidal perturbation of the walls is introduced along the y-direction to provide a selfconsistant source of field error. Details of this can be found in ref.[3]. The initial equilibrium is $B = Bo \tanh(x)$, It has a line of field reversal at x=0 along which reconnection can occur and is maintained by a y-directed electric field and a non-uniform resistivity profile. To produce the plasma flow an initially uniform ExB drift is driven in the y-direction by maintaining a potential diffence between the walls.

To follow the evolution of the plasma in response to the error field, the visco-resistive MHD equations are integrated in time using a semi-implicit, spectral (in y)/ finite diffence (in x)scheme. Since, for the moment, we are only interested in externally driven reconnection the tearing instability is stabilized by reducing the wall separation to $X_w=1$, with Kp=0.35.

Flow Suppression Mechanism

In the absense of flow, the error field induces reconnection of the field lines to form the usual magnetic island structure which generally extends well beyond the reconnection layer. With flow, however, the strong ideal coupling of the field outside the reconnection layer constrains the magnetic field lines to keep the same topology as the fluid flow and so tends to obstruct the further development of the island. A narrow filamentary island is therfore formed within the reconnection layer and dragged partially out of phase with the boundary corrugation by the flow. Since further reconnection is blocked the driving energy of the error field is diverted into shifting the flow out of the magnetic island. Once the flow is removed, however, the island is nolonger topologically constrained and so recontinues its growth, pushing the flow aside as it does. See fig.2(d). Viscous drag causes a finite velocity shear to build up to a maximum around the separatrix of the island. Measurements of the maximum velocity shear, V', over a range of parameters show a clear scaling with viscosity and perturbation amplitude as $V' \propto \delta B\, \nu^{-2/3}$. If we assume, for simplicity, that the flow is only removed from the region of the suppressed island and that its width is equal to the reconnection layer width, Δ_η, then it is clear that the lowest the flow velocity can fall is $\Delta V = 1/2 \Delta_\eta V'$. If the initial flow velocity, V, is greater than ΔV then the island is theoretically unable to proceed and so must remain suppressed. Taking into account conservation of momentum, the critical initial velocity for

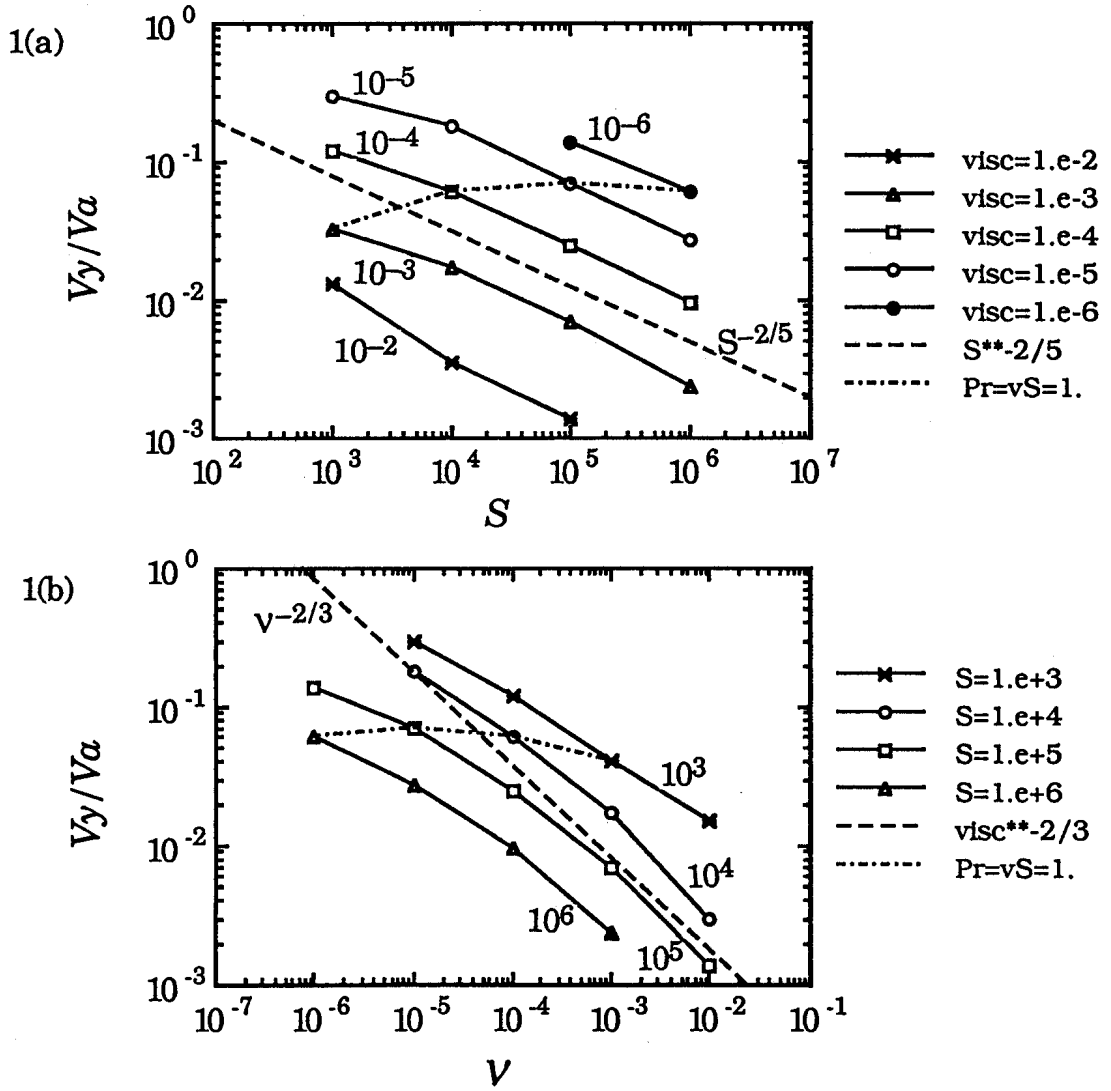

Fig.1 Critical velocity, V_c (a) versus S for different ν and (b) versus ν for different S with $\delta W=0.02$, $X_w=1.$ and $K_p=0.35$. These are compared respectively with the $S^{-2/5}$ and $\nu^{-2/3}$ scalings.of the simple model. Also shows theweak dependence of V_c on S and ν at constant Prandtl number, $P_r=S\nu=1$.

transition to the unsuppressed state should therefore be $V_c = 1/2\Delta_\eta V'(1-1/2\Delta_\eta/X_w)$ where the second term should be negligibly small at small resistivity. From linear theory we know that $\Delta_\eta \propto S^{-2/5}$ so taking this as well as the dependence found for the velocity shear into account we arrive at the scaling: $V_c \propto \delta B\, \nu^{-2/3}\, S^{-2/5}$ where the correction due to momentum conservation has been neglected.

Although the model is an over-simplification of what actually happens it appears to capture the essential features of the mechanism and consequently predicts a scaling for V_c in surprisingly good agreement with the computed dependence on S and δB and to a lesser extent on ν. See figs.1(a) and (b). Runs made with $S=10^4$, $\nu=10^{-4}$, $X_w=1.$, $K_p=0.35$ and $\delta W=0.04$, 0.02, 0.01, 0.005 and 0.0025 for a range of flow velocities showed $V_c \propto \delta W$ to a high precision. Since V' is also $\propto \delta W$ it thus confirms that V_c is affected by the size of the error field directly through the modification of the induced velocity shear.

The intuitive model is too simplistic to correctly predict more than just the general trend in the dependence on viscosity and this is evidenced by the changes in flow cross section observed in the limits of small and large viscosity.

When $\nu\sim\eta$, that is, when the viscous layer width, $\Delta_\nu \sim V/V'$, is roughly equal to the reconnection layer width, Δ_η, the situation is close to that of the intuitive model. See fig.2(b). However when $\Delta_\nu > \Delta_\eta$ the trough in the flow flairs out beyond the reconnection layer, although with the maximum velocity shear still occuring at the edge of the layer as in fig.2(a).

At the other extreme with $\Delta_\nu < \Delta_\eta$, the suppression of the flow is concentrated around the edges of the reconnection layer where the conflict with the flow, due to ideal coupling, is strongest. Thus, instead of one trough, two narrower troughs are formed as shown in fig.2(c). In the centre of the layer, where the resisitivity completely decouples the field from the fluid, the flow is left to pass through the island almost unretarded. The two narrow troughs cannot penetrate as low as a single broader trough with the same velocity shear so a smaller than expected flow velocity is needed to allow the island to become unsuppressed. This change in the flow structure when $\nu \ll \eta$, therefore appears to be why V_c is smaller than that predicted by the scaling of the intuitive-model towards small ν.

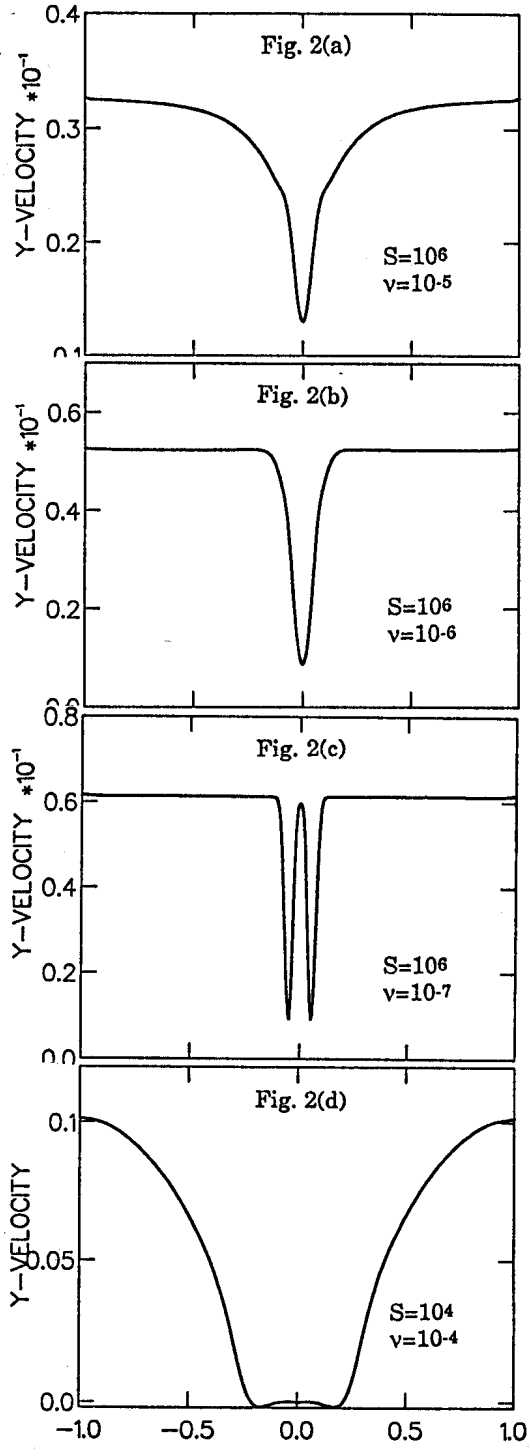

Fig.2 Flow cross-sections for: suppressed islands with Prandtl no. (a) $P_r=S\nu=10.$, (b) $P_r=1.0$,(c) $P_r=0.1$ and (d) for an unsuppressed island.

Time Asymptotic Behaviour

Several interesting features of the saturated behaviour can be seen in fig.3 which shows the transition between the suppressed and unsuppressed states as a function of flow velocity for several different values of the viscosity, and $S=10^3$. The first thing to note is that for sufficiently large viscosity the transition ceases to be discontinuous. This also occurs for large resistivity. To understand this we note that with finite resistivity some relative motion of the

field to the fluid is allowed outside the reconnection layer. The flow therefore does not have to entirely vanish in the island for it to become unsuppressed, It is however only significant for relatively large resistivity. If the viscosity is also large the consequent flair-out of the trough beyond the reconnection layer can allow the island to expand some distance beyond the layer before the flow is made low enough to completely unsuppress the island. The higher the viscosity the more the flow is reduced outside the reconnection layer and so the larger the suppressed island can reach while still in a suppressed state. Eventually for sufficiently large viscosity the flow can be reduced to where the island can reach its unsuppressed size without passing through a discontinuity, as shown in fig.3.

Perhaps the most surprising observation is the flow induced amplification of the unsupressed island well above its zero flow width. This can occur if it is still stable above about 10% of the Alfvén velocity with $\nu<<\eta$. In fig.3, where $S=10^3$, the marginal case occurs for $\nu=10^{-4}$ although this varies depending on the other parameters. As the viscosity is made smaller the amplification begins at a smaller velocity but quickly approaches a limiting case below $\nu=10^{-5}$. This confirms that the amplification only occurs when the flow is a significant fraction of the Alfvén velocity.

Fig. 3

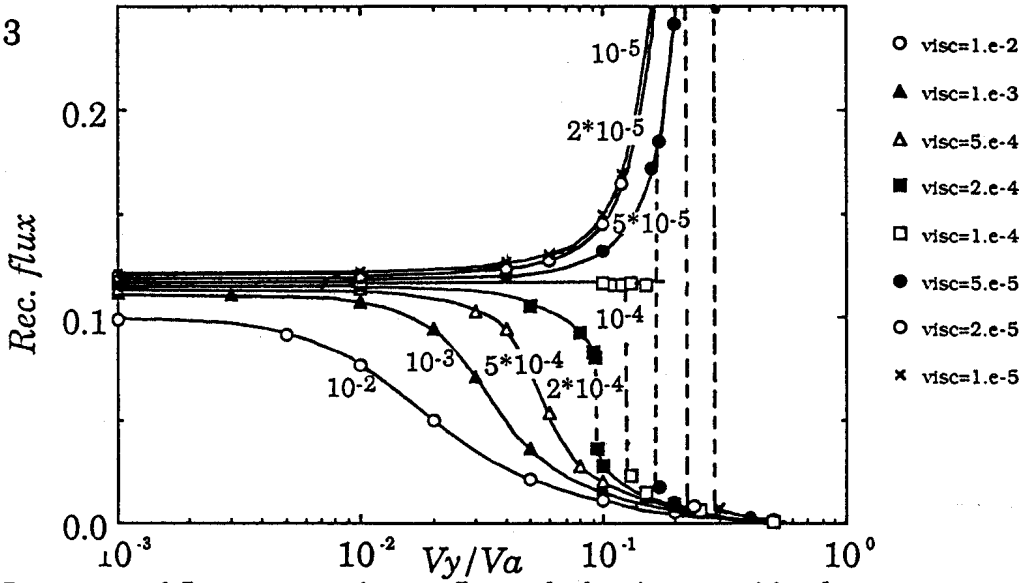

Fig.3 Reconnected flux at saturation vs. flow vel. showing transition between suppressed and unsuppressed islands for different viscosities and $S=10^3$.

Another feature of these flow enhanced states is a form of hysteresis. By restarting a simulation from a solution with $V<V_c$ and slowly increasing the flow at the boundary it is possible to obtain a stable unsuppressed state for $V>V_c$. In effect, there is a finite basin of attraction for the unsuppressed state distinct from that of the the suppressed state. V_c therefore only represents the flow velocity below which the suppressed attractor becomes unstable. A different critical velocity can be defined above which the unsuppressed state becomes unstable.

Changes in the long time behaviour of the suppressed states were also observed. At large S ($S\geq10^5$) and small ν ($\nu\leq10^{-5}$) the supressed island is very narrow and during its evolution it can undergo a spontaneous transition during which secondary islands are formed at the x-points. The increase in the number of islands produces a large rise in reconnected flux without greatly increasing the island width. It tends not to occur, however, in cases where the island eventually becomes unsuppressed.

Acknowledgement: This work was partly supported by the Swiss National Science Foundation.

References

[1] P.R. Thomas et. al., Plasma Phys.& Controlled Fusion,IAEA,Vienna,Vol.1,353,(1985).
[2] J.T. Scoville et. al., Nucl. Fusion, 31, 875, (1991)
[3] R.D. Parker, R.L. Dewar, Comput. Phys. Com., **59**, 1, (1990).
[4] R.D. Parker, PhD Thesis, ANU, Canberra, (1987).
[5] R. Fitzpatrick, T.C. Hender, Phys.Fluids B, **3**, 644, (1991).

Stabilization of Axisymmetric Modes and the Effects of Plasma Deformability in Elongated Tokamak Plasmas Using Active Feedback Coils Inside and Outside the Vacuum Vessel

D. J. Ward, F. Hofmann Centre de Recherches en Physique des Plasmas, Association Euratom–Confédération Suisse, EPFL, Lausanne

In this paper we study the feedback stabilization of the vertical instability in a highly elongated ($\kappa = 3$) TCV plasma using a combination of active coils inside and outside the vacuum vessel. The TCV is a tokamak under construction at the CRPP in Lausanne. It is designed to create plasmas with a variety of cross-sectional shapes with elongations up to $\kappa = 3$. We calculate axisymmetric stability using the NOVA-W code.

In previous studies using NOVA-W [1], it has been shown that the eigenfunction of the axisymmetric mode will be modified under the influence of active feedback in such a way that the effectiveness of the system that detects the vertical displacement by means of magnetic flux measurements is greatly reduced, and thereby the active feedback system becomes less effective or ineffective. In this study we find that fast internal coils very close to the plasma surface can induce an enhanced deformation of the eigenfunction. We shall also demonstrate in this study that a feedback system using a combination of many flux loops and poloidal B-field pickup coils is susceptible to these same problems, and that a large number of distributed flux and B_p measurements used to determine vertical position does not always improve matters.

Figure 1 shows a cross-section of the TCV vacuum vessel, active feedback coils, flux-loops and B_p coils, and the TCV equilibrium used in this study. Also shown are the contours of perturbed plasma flux for the case without active feedback. We are using an equilibrium with a growth rate ($\gamma \approx 6000 s^{-1}$) which is several times faster than the expected operational limit of the growth rate imposed by the power supplies ($\gamma = 2000 s^{-1}$). We choose this more unstable equilibrium because we cannot model all the destabilizing aspects of a real feedback system such as finite bandwidth and voltage limits of power supplies, and because this equilibrium, being very unstable, exhibits very interesting behavior.

There are two active feedback coils inside the vacuum vessel in the corners on the outboard side. There are also 8 active feedback coils outside the vacuum vessel on the outboard side, as well as 8 external coils on the inboard side. The magnetics measurements are composed of a combination of poloidal flux measurements from 38 flux loops just outside the resistive wall (shown in Fig. 1 by an 'X') and poloidal field measurements from 38 B_p-coils just inside the vacuum vessel wall (each is noted by 'c'). These measurements can be used in any combination as a way to determine the vertical position of the plasma as input for the feedback system. In this study we number the flux-loop, B_p-coil pairs (which are up-down symmetric about the midplane) from #1 at the inboard midplane to #20 at the outboard midplane. The numbering is shown in Fig. 1. We use a two time-scale feedback system [2] using both the internal and external active coils. The voltage applied to the internal coils is equal to some gain (proportional plus derivative) multiplied by a measure of the vertical displacement which is composed of a combination of perturbed flux and B_p measurements. The voltage applied to the external coils is proportional to the current in the internal coils. In the case we consider first, the voltages applied to all external coils are of the same magnitude. The internal coils provide the fast response necessary to stabilize these highly elongated plasmas, but they have power limitations, so this two stage system allows the current in the fast internal coils to return to zero by replacing their stabilizing force by that of the more powerful, but slower, external coils.

Figure 2 shows the plot of perturbed flux for the TCV plasma under active feedback using all feedback coils (internal and external). When the complete set of flux loops are used (but no B_p measurements) the plasma cannot be made stable with this coil configuration. This is due to the fact that the sum of the flux-loop signals goes to zero as the feedback gain is increased to large values. In Ref. [1] it was shown that the deformation of the eigenfunction under active feedback can cause the measured signal at a pair of flux loops to go to zero, rendering the feedback system ineffective. We see here that using a combination of a large number of flux-loop measurements does not necessarily improve matters. The contour of zero-flux is shown as a dotted line in Fig. 2. The flux loops inside this contour measure positive flux, while those outside measure negative flux. It is not necessary that the flux be zero at *each* of the detector pairs for the feedback system to be made ineffective, but only that the measured fluxes add positive and negative values to give an *overall sum* that decreases at the same rate that the gain increases. In this configuration, a relatively small modification of the eigenfunction is sufficient to make the sum of the flux measurements go to zero as the gain is increased to large values.

It is apparent from the fact that the zero-flux contour in Fig. 2 lies so close to most of the flux loops that most pairs of flux loops if used by themselves would be ineffective. However, a single pair of well placed flux loops can be better than the complete set that surrounds the plasma. An example of an *effective* single pair of flux loops is pair #17. Comparing Fig. 1 and Fig. 2 we see that the influence of the internal coils induces a deformation in the eigenfunction that produces a bulge in the perturbed flux to the outboard side. This in turn increases the detected flux signal at these flux loops. In

Figure 1

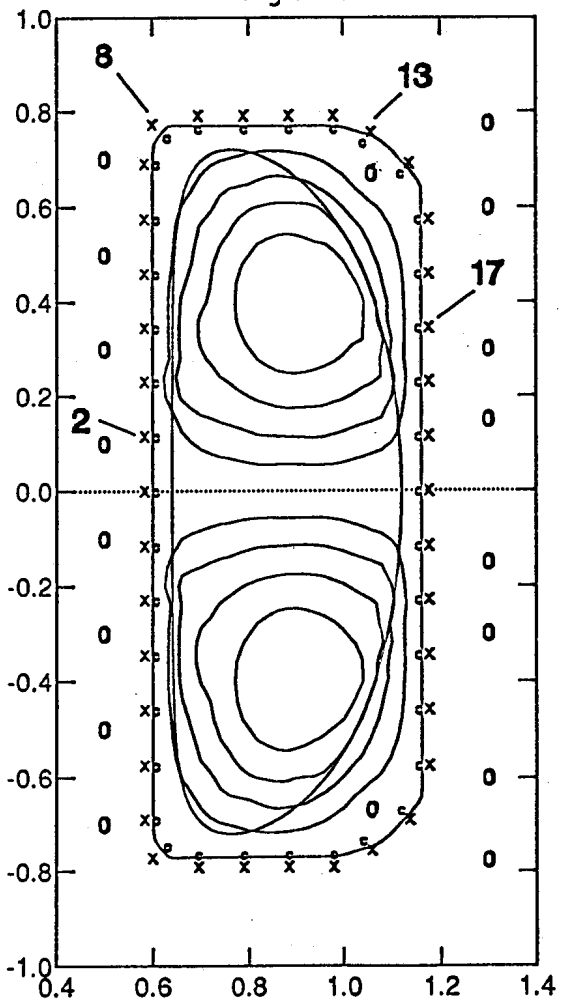

Figure 2

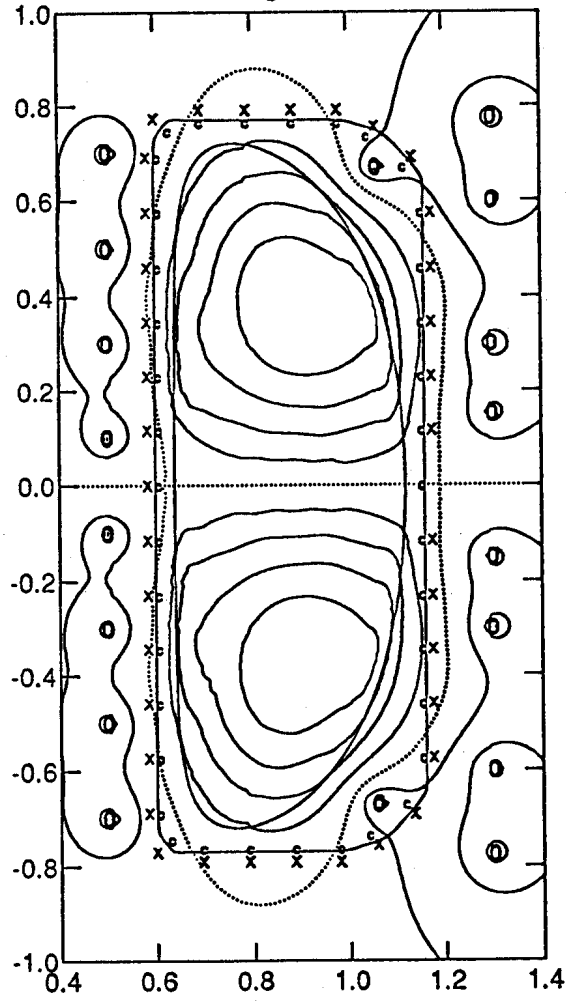

this case one can take advantage of the deformation in the eigenfunction due to the influence of the internal coils to use flux loops that would be quite ineffective without this deformation. The flux-loop pairs that are effective when used by themselves are at positions #10, #11, #17, #18, and #19.

When the complete set of B_p-coils are added to the set of flux loop measurements in a weighted sum [3], the plasma can be stabilized with the active feedback system described above. The deformation of the eigenfunction under the influence of the feedback system is unable to make the sum of the magnetic measurements go to zero. In fact, if the measurement from the corresponding pair of B_p-coils is added to the measurement from a single pair of the flux loops, the combination is effective for *most* of the pairs. However this is not true in all cases, and one must still be careful in choosing the location of the flux-loop, B_p-coil pairs. In some cases the sum of a negative flux measurement plus a positive B_p measurement yields a null signal. The *ineffective* locations for the single flux-loop, B_p-coil pairs are at positions #7, #8, #9, #12, #13, #14, and #15.

We find that the deformation of the eigenfunction due to active feedback is virtually the same when flux-loop pair #17 is alone used as when the complete set of flux-loop and B_p-coil measurements is used for this case. This is quite different from previous results for the PBX-M configuration [1]. This appears to be due to the fact that the active feedback system using internal coils and many nearby external coils on both the inboard and outboard sides imposes a particular deformation of the eigenfunction that is not significantly affected by this change in the detection system. This is not necessarily the case if the distribution of the coil currents in the active coils were changed.

The effectiveness of a particular feedback system is very sensitive to the distribution of currents in the active coils. Changing the relative weights of the feedback gains on the various coils changes the eigenfunction, and it changes the way that the eigenfunction can be deformed in order to defeat the detection system. In the feedback system used in Fig. 2 there is a voltage of equal magnitude applied to all external coils. Now we consider calculations where the voltages on the external coils are weighted such that the voltage applied to the coils farther away from the midplane is proportionately higher than the voltage applied to those close to the midplane, and the voltage applied to the inboard coils is smaller than that applied at the outboard coils. With this weighting of the voltages the resulting currents in the external coils provide a more uniform radial field inside the vacuum vessel.

This completely changes the deformation of the eigenfunction under active feedback, and it is such that the detection system using the full configuration of flux-loops and B_p-coils is no longer effective. Figure 3 shows the ways that the eigenfunction changes under the effect of the different coil current distributions. In Fig. 3 we show the ratios of the m^{th} poloidal harmonic of the radial component of the eigenfunction to the first harmonic, $\xi_{\psi m}/\xi_{\psi 1}$, at the plasma edge for $m = 2, 3, 4$. These are displayed versus the corresponding growth rate, γ, for that case. The feedback gain is increasing as the growth rate decreases, i.e., it is increasing as one moves to the left along the curves. The ratios $\xi_{\psi m}/\xi_{\psi 1}$ are shown for three cases. The first case (case A) uses the combination of internal and external coils with equal voltage applied to the external coils as in the case shown in Fig. 2. The second case (case B) has only the external coils activated (with equal weighting) and the internal coils remain passive, and the third case (case C) uses a combination of internal and external coils with the voltages on the external coils weighted in order to give a more uniform radial field as discussed above. All three cases use a detection system using the full combination of all flux-loops and B_p coils shown in Fig. 2. In each case the ratios for $\xi_{\psi 2}/\xi_{\psi 1}$ are shown by squares,

the ratios for $\xi_{\psi 3}/\xi_{\psi 1}$ are shown by circles, and the ratios for $\xi_{\psi 4}/\xi_{\psi 1}$ are shown by triangles (case A by small open symbols, case B by solid symbols, and case C by large open symbols).

The difference in the deformation of the eigenfunction is quite clear between these three cases. For example, the values for $\xi_{\psi 2}/\xi_{\psi 1}$ for case A evolve with increasing gain (decreasing growth rate) in the opposite direction to the other two cases. Likewise, the values for $\xi_{\psi 3}/\xi_{\psi 1}$ for case B evolve in the opposite direction from the other cases. For case B and case C the deformation is such that the plasma cannot be made stable. The total magnetic measurement of the vertical displacement goes to zero at the same rate that the gain is increased. Increasing the gain only serves to further modify the eigenfunction. The plasma in case A can be made stable (points to the left of the vertical line in Fig. 3), but the eigenfunction changes to a large extent after the plasma becomes stable, and the magnitude of the stable eigenvalue seems to be limited.

CONCLUSION

We see that the deformation of the eigenfunction plays a crucial role in the ability of the feedback system to successfully stabilize the plasma. It is important to understand the deformation of the eigenfunction resulting from a particular choice of active coils in order to choose an appropriate set of magnetic measurements to determine the vertical displacement. The use of internal and external active coils imposes a particular deformation that allows one to choose a small number of well placed measurements. A large number of magnetic measurements distributed around the plasma does not necessarily improve matters, and in fact can be much less effective than a small number of well placed measurements. The deformation of the eigenfunction is also strongly affected by the distribution of currents in the external coils.

[1] D. J. Ward and S. C. Jardin, LRP 434/91, CRPP-EPFL, Lausanne (September 1991). To appear in Nucl. Fusion **32** (1992) #6 or #7.

[2] F. B. Marcus, F. Hofmann, S. C. Jardin, et al., Nucl. Fusion **30** (1990) 1511.

[3] F. Hofmann and G. Tonetti, Nucl. Fusion **28** (1988) 519.

Figure 3